Computational Materials Science 48 (2010) 842–847

Contents lists available at ScienceDirect

Computational Materials Science

journal homepage: www.elsevier.com/locate/commatsci

Finite element analysis of oxidation induced metal depletion at oxide–metal interface

Honggang Zhou [a], Jianmin Qu [a,b], Mohammed Cherkaoui [a,b,*]

[a] School of Mechanical Engineering, Georgia Institute of Technology, Atlanta, GA 30322-0405, United States
[b] UMI 2958 GT-CNRS, Metz 57000, France

ARTICLE INFO

Article history:
Received 30 October 2009
Received in revised form 1 February 2010
Accepted 25 March 2010

Keywords:
Cr–Fe alloys
Oxidation
Stress
Finite element
Voronoi tessellation

ABSTRACT

In many situations, chromium depletion and voiding below oxide/alloy interface accompany with the selective oxidation of Cr–contained alloys. At the same time, stresses are induced at the oxide/alloy interface, in the metal and in the oxide. The combination of depletion and stress generation initiates interfacial crack-like voids which eventually lead to spallation of the oxide scale. In this paper, a continuum thermodynamic model which accounts for stress-diffusion interaction in the oxidation of Cr–Fe alloys is carried out via a two-dimension finite element implementation. For the purpose of generating depletion areas, grain areas and grain boundary areas in the alloy are defined via random Voronoi tessellation. Periodic boundary condition is also employed. The model predicts that the depletion of chromium mostly occurs at the fast diffusion area (grain boundary), and large normal tensile stresses are generated at both metal-scale interface and alloy grain boundaries. Once the depletion-induced voids reaches a certain level at the interface, concentration of stress could induce further propagation of interfacial crack.

Published by Elsevier B.V.

1. Introduction

Formation of a layer of oxide (e.g. Cr_2O_3) on alloy surfaces helps to protect alloy from further degradation in high temperature oxidizing environment. One of the most encountered problems with the oxide layers is their spallation during extending service limits the lifetime of alloy parts in many applications. This phenomenon has drawn researchers' attention in the last several decades. The consequences of both observations of mechanisms and theoretical modeling attribute the origins of spallation to two aspects.

Residual stresses, especially those of chemical nature [1–3] are believed to be one of the factors that cause oxide layer spall off. Some attempts have been made to develop computational models to describe the oxidation-stress interaction process [4–6]. Most of the existing models are based on the original concept of Rhines and Wolf [2]. Clarke [4] considered the generation of lateral growth strain in response to the counter-diffusion of cations and anions. By neglecting stress relaxation, they shown that the lateral growth strain rate is proportional to the outward cation flux. Under a steady-state condition, Limarga et al. [5] derived the average growth stress by assuming that the inward oxygen diffusion occurs along grain boundaries. A more general model describing the stress and composition fields in the oxide scale is presented by Zhou et al. [6], in which they had formulated a continuum framework that predicts the spatial distribution of stress and concentrations within the oxide scale. The stresses affect internal oxidation by changing the free energy of the reaction and affect diffusion by modifying the chemical potential. This allows the authors to consider how the stress inhibits internal oxidation in a thermodynamically and kinetically consistent manner.

On the other hand, spallation of protective oxide layer is associated with metal depletion effects [7–9] at the oxide layer/alloy interfaces. Seo et al. [9] observed a Cr-depletion zone in their study on selective oxidation of Fe–Cr alloy in pure oxygen, and concluded that the transport of Cr in the oxide film contributes to the formation of Cr-depletion zone. A deeper observation at the metal–oxide interface made by Howes [7] shows that the most severe depletions occur at the grain boundaries (Figs. 1a and 1b). Modeling the solute depletion process usually employs solving the diffusion equations through the sample volume. Since depletion is the only modeling object, stress profile around the interface is not included. On the other hand the aforementioned residual stress models are all for 1D geometry and did not consider possible metal depletion effect. So in this study, we aim to apply a general stress-diffusion coupled model in 2D geometry with specific interests in metal depletion at alloy grain boundaries and their adjacent stress distribution during the selective oxidation of Cr–Fe alloys.

* Corresponding author at: School of Mechanical Engineering, Georgia Institute of Technology, Atlanta, GA 30322-0405, United States. Tel.: +1 33 3 87 20 39 36; fax: +1 404 894 8336.
E-mail address: mohammed.cherkaoui@me.gatech.edu (M. Cherkaoui).

0927-0256/$ - see front matter Published by Elsevier B.V.
doi:10.1016/j.commatsci.2010.03.044

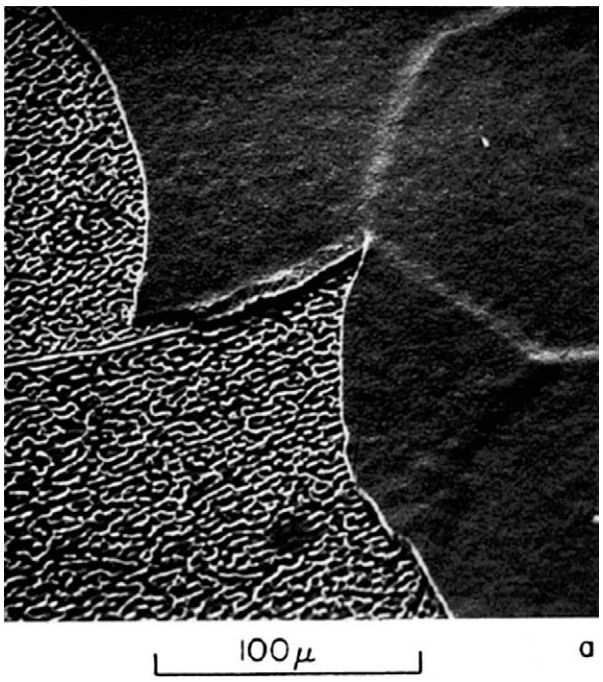

Fig. 1a. Oxide and the alloy surface after partial spalling [7].

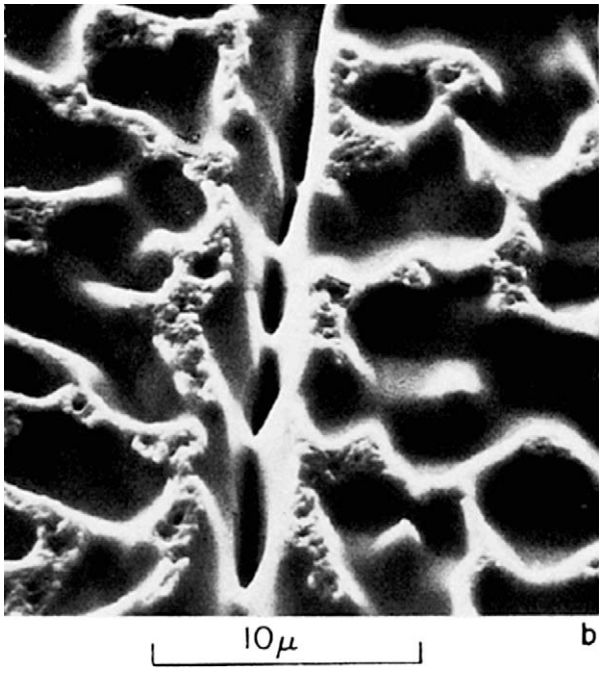

Fig. 1b. Sorrugated alloy surface and the crevasses formed at a grain boundary [7].

2. Model description

2.1. Voronoi tessellation

Voronoi tessellation is a well established method to represent polycrystalline solid models. In a Voronoi tessellation spaces, 'seed points' (represented by P_i) are randomly distributed in space (3D) or plane (2D). All other points in the space that are close to a 'seed point' than any other 'seed points' is grouped as a region which defines the Voronoi tessellation. For 2D space, Voronoi tessellation divides the space into an array of convex, space filling polygon. The mathematical description of Voronoi tessellation is given as

$$\boldsymbol{V}_i = \{x_i : d(x_i, P_i) \leqslant d(x_i, P_j); \quad i \neq j; \quad i, j = 1, 2, 3, \ldots, n\}, \tag{1}$$

where $\boldsymbol{V}_i$ represents a grain set, x_i denotes a random point in the space, $d(x_i, P_i)$ is the distance between P_i and x_i, n represents the total number of points in the space.

The most advantage of Voronoi tessellation is that it has been extensively used to characterize the grain aggregation, grain boundary phenomena. Kumar and Kurtz [10] used a 3D Voronoi tessellation to calculate the effective thermal expansion coefficient of polycrystalline materials. Microscopic based macroscopic material behavior modeling with Voronoi tessellation is not only limited in this, but also in creep fracture [11], constitutive relations [12,13] and electrical conductance [14] and many other areas. On the other hand, Voronoi tessellation has also been used for research on local phenomena, especially those at grain boundaries. For example, Kamaya and Itakura [15] generated a 3D polycrystalline body with Voronoi tessellation to study intergranular crack initiation and propagation, as well as the stress concentration around the cracks.

It deserves to notice that using Voronoi tessellation to describe polycrystalline solids is under the following assumptions [16]:

1. Grain growth starts at all points P_i in a finite set of nuclei $\boldsymbol{V}_i$ (referred to as 'seed point') at the same time. The nuclei are fixed at their spatial position during the growth process, i.e. they do not move.
2. Isotropic and uniform grain growth. Particularly, the velocity of the grain growth is assumed to be equal in:
(a) all grains and
(b) all directions.
3. Grain growth in a direction stops as two grain boundaries contact each other, i.e. there is no grain overlapping. The growth process stops, if there is not any further grain growth in any direction in any grain.
4. There are no voids, i.e. the entire volume is populated by grains.

2.2. Diffusion-stress coupling

The selective oxidation process of Cr–Fe alloy is modeled by a continuum thermodynamic model accounting for stress-diffusion interaction [6]. This model accounts for the stress-diffusion interaction by including a stress dependent term in the chemical potential of diffusible species. It describes well the oxidation process and has a good agreement with experiments on oxidation kinetics behavior of Cr–Fe alloy.

Chemical potential, the quantities governed the ionic diffusion is given as [6]

$$\mu_s = \mu_s^0 + RT \ln c_s + V_s^m \tau_s, \tag{2}$$

where μ_s^0 is the chemical potential of species s at some reference state, R and T are the universal gas constant and temperature, respectively, V_s^m is the molar volume of species s in its nature state (stress-free stoichiometric state). The last term in (2) is the stress-dependent part of the chemical potential, for constant linear elastic and small strain deformation

$$\tau_s = \eta_s \left(\frac{3}{2} C_{ijkl}^0 \varepsilon_{ij}^E \varepsilon_{kl}^E - \sigma_{kk} \right), \tag{3}$$

where η_s is the coefficients of compositional expansion, C_{ijkl}^0 are the elastic constants, ε_{ij}^E is the elastic strain, σ_{kk} is the trace of the Cauchy stresses. In Eq. (3), the summation convention is adopted.

2.3. Model of polycrystalline Cr–Fe alloy with oxide

Fig. 2a illustrates the geometry of a polycrystalline alloy carrying an initial Cr_2O_3 at its top surface. The 2D model (Fig. 2b) studied in this paper is a piece of sample cut between the dash line as shown in Fig. 2a. The oxide scale is assumed to be homogeneous and isotropic with an initial thickness. Both figures are only for illustration purpose not to scale.

Interfacial voiding in the alloy is an ineluctably phenomenon accompanying the selective oxidation process from the very beginning. However, it might takes a relative long time of oxidation for the voids to grow up to a certain size such that they could become harmful to the oxide-alloy adherence, such as spallation. In this study, we assume that steady state of oxidation has been reached before voiding becomes harmful at oxide/alloy interface. So we only focus on steady state oxidation in this study. It should be noted here that steady state oxidation does not imply time independence. For oxidation kinetics, steady state means that the relationship between oxide thickness and time obeys the parabolic law, this has been well acknowledged since Wagner [17].

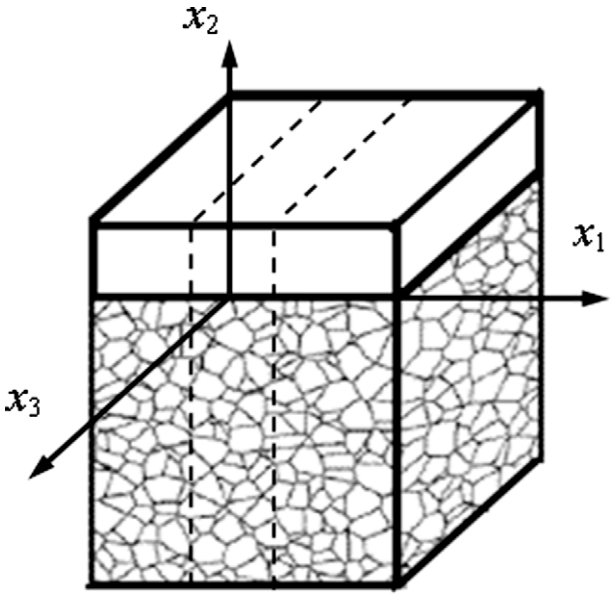

Fig. 2a. 3D Structure of polycrystalline alloy carrying a layer of oxide.

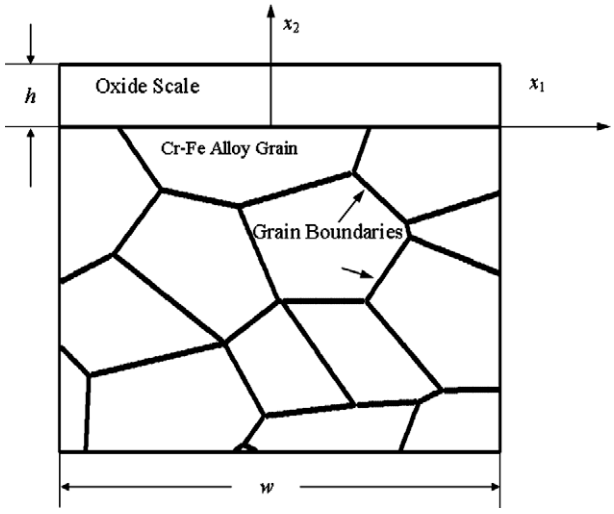

Fig. 2b. 2D Structure of polycrystalline alloy carrying a layer of oxide.

Even though it was assumed that oxide formation can occur all over the oxide, a 1D example in [6] shows that when oxidation kinetics reaches steady state, the oxide only forms at the surface (oxide/oxygen phase boundary), which, is consistent with the assumption of many classical approaches [6,17–19]. Based on this result, we assume that chemical equilibrium established between reactants (cations and anions) and product (oxide) inside the oxide bulk. Therefore, below the reaction active surface, there is no dramatic strain increase due to increase of lattice sites in the oxide. Hence, the small deformation assumption can be applied to the model in [6] instead of the finite deformation to reduce the calculation complexities.

From [6], deformation and defect concentration throughout the oxide scale layer and alloy substrate can be solved from the corresponding governing partial differential equations with proper continuity conditions. For this two dimensional model in current study, the equilibrium equations

$$\begin{aligned}\frac{\partial\sigma_{11}}{\partial x_1}+\frac{\partial\sigma_{12}}{\partial x_2}&=0,\\ \frac{\partial\sigma_{21}}{\partial x_2}+\frac{\partial\sigma_{22}}{\partial x_1}&=0,\end{aligned}\tag{4}$$

have to be satisfied both in oxide and in alloy substrate. The mass continuity equations for Cr and O ions in oxide scale are given as

$$\begin{aligned}\frac{\partial c_{\mathrm{Cr}}}{\partial t}&=D_{\mathrm{Cr}}\left[\frac{\partial}{\partial x_1}\left(\frac{\partial c_{\mathrm{Cr}}}{\partial x_1}+c_{\mathrm{Cr}}\frac{V^m_{\mathrm{Cr}}}{RT}\frac{\partial\tau_{\mathrm{Cr}}}{\partial x_1}\right)+\frac{\partial}{\partial x_2}\left(\frac{\partial c_{\mathrm{Cr}}}{\partial x_2}+c_{\mathrm{Cr}}\frac{V^m_{\mathrm{Cr}}}{RT}\frac{\partial\tau_{\mathrm{Cr}}}{\partial x_2}\right)\right],\\ \frac{\partial c_{\mathrm{O}}}{\partial t}&=D_{\mathrm{O}}\left[\frac{\partial}{\partial x_1}\left(\frac{\partial c_{\mathrm{O}}}{\partial x_1}+c_{\mathrm{O}}\frac{V^m_{\mathrm{O}}}{RT}\frac{\partial\tau_{\mathrm{O}}}{\partial x_1}\right)+\frac{\partial}{\partial x_2}\left(\frac{\partial c_{\mathrm{O}}}{\partial x_2}+c_{\mathrm{O}}\frac{V^m_{\mathrm{O}}}{RT}\frac{\partial\tau_{\mathrm{O}}}{\partial x_2}\right)\right],\end{aligned}\tag{5}$$

and for Cr atom in alloy substrate

$$\begin{aligned}\frac{\partial c_{\mathrm{Cr}(a)}}{\partial t}=D_{\mathrm{Cr}(a)}\Bigg[&\frac{\partial}{\partial x_1}\left(\frac{\partial c_{\mathrm{Cr}(a)}}{\partial x_1}+c_{\mathrm{Cr}(a)}\frac{V^m_{\mathrm{Cr}(a)}}{RT}\frac{\partial\tau_{\mathrm{Cr}(a)}}{\partial x_1}\right)\\ &+\frac{\partial}{\partial x_2}\left(\frac{\partial c_{\mathrm{Cr}(a)}}{\partial x_2}+c_{\mathrm{Cr}(a)}\frac{V^m_{\mathrm{Cr}(a)}}{RT}\frac{\partial\tau_{\mathrm{Cr}(a)}}{\partial x_2}\right)\Bigg],\end{aligned}\tag{6}$$

where D_s is the diffusivity of species s in corresponding diffusion media (s = Cr, O in oxide, $s = \mathrm{Cr}_{(a)}$ in alloy).

With chemical reaction equilibrium assumption, we have

$$d\mu_p-2d\mu_{\mathrm{Cr}}-3d\mu_{\mathrm{O}}=0,\tag{7}$$

where μ_{Cr}, μ_{O} and μ_p are, respectively, the chemical potentials of Cr and O ion, as well the product Cr_2O_3

Since the alloy grains and grain boundaries are randomly distributed and oriented, the material we studied in the model is assumed to be isotropic. So the non-zero stress and elastic strain components are given as

$$\begin{aligned}\sigma_{11}&=\frac{E}{(1+\nu)(1-2\nu)}\left[(1-\nu)\left(\frac{\partial u_1}{\partial x_1}-\sum_s\eta_s\Delta c_s\right)+\nu\left(\frac{\partial u_2}{\partial x_2}-2\sum_s\eta_s\Delta c_s\right)\right],\\ \sigma_{22}&=\frac{E}{(1+\nu)(1-2\nu)}\left[(1-\nu)\left(\frac{\partial u_2}{\partial x_2}-\sum_s\eta_s\Delta c_s\right)+\nu\left(\frac{\partial u_1}{\partial x_1}-2\sum_s\eta_s\Delta c_s\right)\right],\\ \sigma_{33}&=\frac{E}{(1+\nu)(1-2\nu)}\left[(1-\nu)\left(-\sum_s\eta_s\Delta c_s\right)+\nu\left(\frac{\partial u_2}{\partial x_2}-\sum_s\eta_s\Delta c_s\right)\right.\\ &\quad\left.+\nu\left(\frac{\partial u_1}{\partial x_1}-\sum_s\eta_s\Delta c_s\right)\right],\\ \sigma_{12}&=\frac{E}{2(1+\nu)}\left(\frac{\partial u_1}{\partial x_2}+\frac{\partial u_2}{\partial x_1}\right)\end{aligned}\tag{8}$$

and

$$\begin{aligned}\varepsilon^E_{dd} &= \frac{\partial u_1}{\partial x_1} - \sum_s \eta_s \Delta c_s,\\ \varepsilon^E_{22} &= \frac{\partial u_1}{\partial x_2} - \sum_s \eta_s \Delta c_s,\\ \varepsilon^E_{33} &= -\sum_s \eta_s \Delta c_s,\\ \varepsilon^E_{12} &= \frac{1}{2}\left(\frac{\partial u_1}{\partial x_2} + \frac{\partial u_2}{\partial x_1}\right).\end{aligned} \tag{9}$$

In addition to the governing equations above, interface conditions need to be specified. In the structure shown in Fig. 2b, there are two interfaces, the metal-scale interface and the scale-air interface. At these interfaces, the following conditions must be satisfied: (a) mass flux continuity of each species, (b) continuity of chemical potential of each species for adsorption and ionization reaction, respectively, (c) continuity of displacement and (e) continuity of traction. These conditions are described below.

2.3.1. Metal-scale interface ($x_2 = 0$)

At the metal-scale interface, ionization of Cr atoms is assumed to be an equilibrium process. Thus, continuity of chemical potentials must hold between Cr ions and Cr atoms, i.e.

$$\frac{\mu^0_{\mathrm{Cr}(a)} - \mu^0_{\mathrm{Cr}}}{RT} + \ln\frac{c_{\mathrm{Cr}(a)}}{c_{\mathrm{Cr}}} = \frac{V^m_{\mathrm{Cr}}\tau_{\mathrm{Cr}} - V^m_{\mathrm{Cr}(a)}\tau_{\mathrm{Cr}(a)}}{RT}. \tag{10}$$

Conservation of mass for Cr across the interface leads to

$$\frac{\partial c_{\mathrm{Cr}(a)}}{\partial x_2} + \frac{V^m_{\mathrm{Cr}(a)} c_{\mathrm{Cr}(a)}}{RT}\frac{\partial \tau_{\mathrm{Cr}(a)}}{\partial x_2} = \frac{D_{\mathrm{Cr}}}{D_{\mathrm{Cr}(a)}}\left[\frac{\partial c_{\mathrm{Cr}}}{\partial x_2} + \frac{V^m_{\mathrm{Cr}} c_{\mathrm{Cr}}}{RT}\frac{\partial \tau_{\mathrm{Cr}}}{\partial x_2}\right]. \tag{11}$$

Furthermore, per the assumption that no O can cross the interface into the metal, i.e.,

$$\frac{\partial c_{\mathrm{O}}}{\partial x_2} + \frac{V^m_{\mathrm{O}} c_{\mathrm{O}}}{RT}\frac{\partial \tau_{\mathrm{O}}}{\partial x_2} = 0. \tag{12}$$

Finally, traction continuity is automatically satisfied by the choice of stress components, and the continuity of displacement leads to

$$u_1|_{x_2=0^+} = u_1|_{x_2=0^-}, \quad u_2|_{x_2=0^+} = u_2|_{x_2=0^-}. \tag{13}$$

2.3.2. At the scale-air interface ($x_2 = h$)

At the scale-air interface, equilibrium condition is assumed for ionization of oxygen (in the air), i.e.,

$$\frac{1}{2RT}\mu^0_{\mathrm{O}_2} + \ln P^{1/2}_{\mathrm{O}_2} = \frac{\mu^0_{\mathrm{O}}}{RT} + \ln c_{\mathrm{O}} + V^m_{\mathrm{O}}\tau_{\mathrm{O}}. \tag{14}$$

where $\mu^0_{\mathrm{O}_2}$ is the standard chemical potential of oxygen gas and P_{O_2} is the oxygen partial pressure in the air. Note that h is not known a priori. It is a function of time that needs to be solved. In addition, since the oxide forms at the surface and Cr ions cannot leave the scale, the Cr ion flux all transform to oxide and must follow the Stefan [19] condition at the scale-air interface, i.e.,

$$\frac{V^m_p}{2} D_{\mathrm{Cr}}\left(\frac{\partial c_{\mathrm{Cr}}}{\partial x_2} + \frac{V^m_{\mathrm{Cr}} c_{\mathrm{Cr}}}{RT}\frac{\partial \tau_{\mathrm{Cr}}}{\partial x_2}\right) = -\frac{du_2}{dt}. \tag{15}$$

Furthermore, it is assumed that, in comparison with the stresses in the scale layer, the atmosphere pressure is negligible in typical applications. Thus, the scale-air interface can be viewed as a traction free surface which is satisfied by the choice of the stress components.

Inside the alloy far from the interface, $c_{\mathrm{Cr}(a)} = C$ as $x_2 \to -\infty$. Additionally, periodic boundaries are applied at the left ($x_1 = -\frac{w}{2}$) and right ($x_1 = \frac{w}{2}$) hand side of the 2D model, i.e.,

Table 1
Material properties of 16% Cr–Fe alloy and its oxide.

Chromia properties	Symbol	Value
Chemical expansion coefficient	η_{Cr}	0.05
	η_{O}	0.02
	η_p	5/3
Diffusivity of chromium ion	D_{Cr}	5.8×10^{-13} cm^2/s
Diffusivity of oxygen ion	D_{O}	3.0×10^{-15} cm^2/s
Temperature	T	1073 K
Young's modulus	E	250 GPa
Poisson's coefficient	ν	0.27
Molar volume	V^m_p	2.92×10^{-5} m^3/mol
16% (wt) Cr–Fe alloy properties		
Chemical expansion coefficient	$\eta_{\mathrm{Cr}(a)}$	0.05
Diffusivity of chromium atom	$D_{\mathrm{Cr}(a)}$	2.86×10^{-15} cm^2/s in grain volume 1.57×10^{-13} cm^2/s in grain boundary
Young's modulus	E	162.3 GPa
Poisson's coefficient	ν	0.29

$$\begin{aligned}&u_1|_{x_1=-\frac{w}{2}} = u_1|_{x_1=\frac{w}{2}}, \quad u_2|_{x_1=-\frac{w}{2}} = u_2|_{x_1=\frac{w}{2}}\\ &c_{\mathrm{Cr}}|_{x_1=-\frac{w}{2}} = c_{\mathrm{Cr}}|_{x_1=\frac{w}{2}}, \quad c_{\mathrm{O}}|_{x_1=-\frac{w}{2}} = c_{\mathrm{O}}|_{x_1=\frac{w}{2}}, \quad c_{\mathrm{Cr}(a)}|_{x_1=-\frac{w}{2}} = c_{\mathrm{Cr}(a)}|_{x_1=\frac{w}{2}}.\end{aligned} \tag{16}$$

This stress-diffusion coupled model for steady state oxidation of 16% (wt) Cr–Fe alloy was implemented by finite elements in commercial software ABAQUS with a user-defined element subroutine. The material properties of 16% (wt) Cr–Fe alloy and its oxide used in the numerical simulation are listed in Table 1. Oxygen partial pressure is set to be 0.3 atm at the air-oxide interface. Elements in the alloy part are divided into sets of grains and grain boundaries based on random Voronoi tessellation diagram. Elements beyond the oxide/alloy interface are grouped into two sets, the oxide and air which are separated by the oxide/gas surface. These elements are with fine mesh and identical in thickness in x_2 direction. The oxide scale surface moving is calculated by integrating Eq. (15). When the displacement at the oxide surface layer exceed the specified element thickness, the material properties of the upper layer of elements at the air side switch from those for air to oxide.

3. Results and discussions

Results about the oxidation kinetics are shown in Figs. 3a and 3b for the purpose of validation of the models. Changes of oxide scale thickness versus normalized sample width at different time are plotted in Fig. 3a. As can be seen, the top surface of oxidation is flat. From the thickness strategy in last section, this means that local thickness difference is less than the thickness of an element in x_2 direction. So we may approximately consider the oxide with a uniform thickness. Comparison between the numerical prediction and experimental results [20] at steady state given in Fig. 3b agrees with each other very well, which shows that this model with small deformation assumption is valid.

Under many circumstances, spallation of Cr_2O_3 scale starts with depletion of Cr metal oxide/alloy interface. Faster diffusion rate of Cr in oxide than in binary alloy is the mechanism to explain this phenomenon. Fig. 4 shows the contours of Cr concentration in the alloy after the oxidation time of 200 h. The minus value of Y axis represents the distance below the metal–oxide interface where the coordinate origin locates. Decreasing of Cr concentration at the alloy side of the interface is observed and the most dramatic change of Cr content is located at two grain boundary areas. Since the grain boundary diffusivities are over 2 orders higher than those

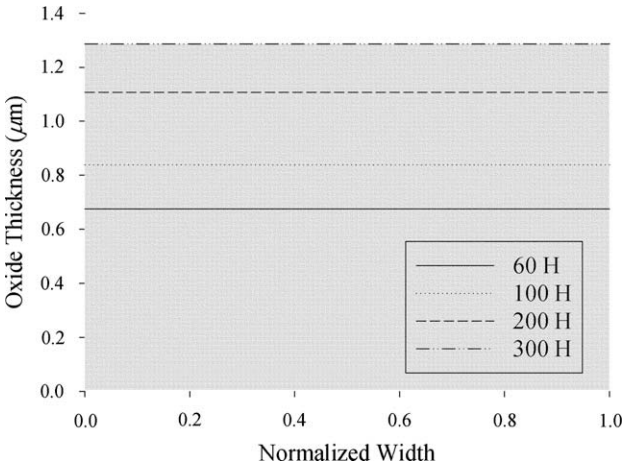

Fig. 3a. Growth of oxide thickness with time in 2D.

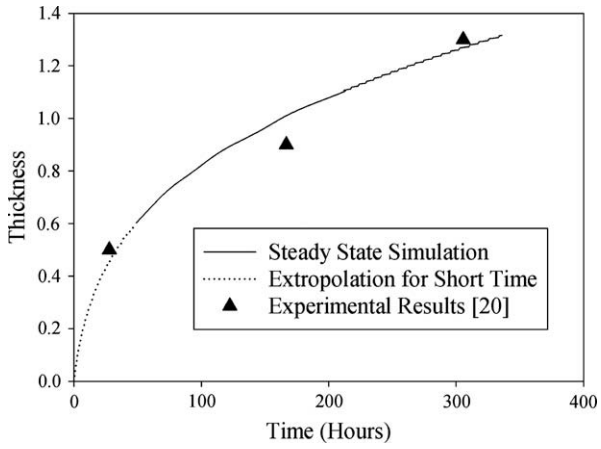

Fig. 3b. Comparison of growth of oxide between simulation and experiment results.

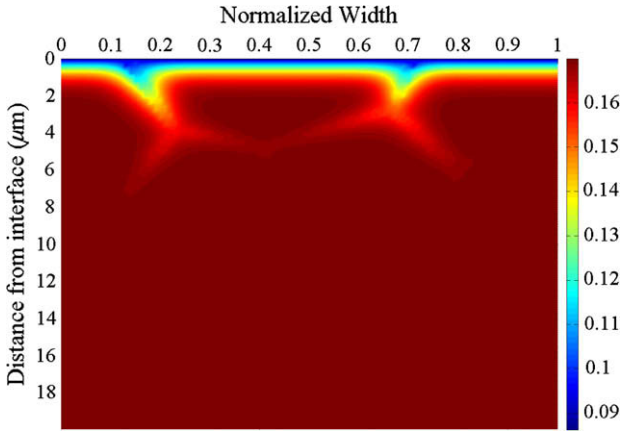

Fig. 4. Contour of Cr concentration in the alloy after the oxidation time of 200 h.

of grain bulk, Cr atoms are easier moves in grain boundaries. Hence more Cr atoms leave to oxide scale from alloy grain boundaries leads to lower local concentration. Accordingly, in the oxide, higher Cr ion concentration could be located at the areas adjacent to alloy grain boundaries (Fig. 5). Depletion of Cr at grain not only reduces

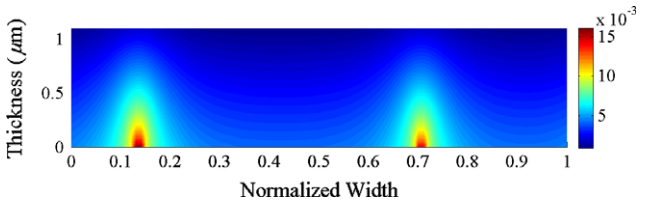

Fig. 5. Contour of Cr concentration in the oxide after the oxidation time of 200 h.

the local mass density of the alloy, but enables the generation of other lower dense product. For example, oxidation of low Cr content Fe–Cr alloy would have Fe contained product (e. g. $(Fe, Cr)_3O_4$), which could lead to loose and incompact oxide layer and consequently be easy to peel off and decompose.

Stresses generated due to changes of species concentration are important driven forces that cause interfacial failure. Fig. 6 shows the contours of in plane stress σ_{11} in oxide and alloy after 200 h of oxidation. It can be seen that compressive in plane stresses are generated in most area of the oxide and reach maximum value adjacent to the alloy grain boundary. Relatively high local Cr ion concentrations at these areas allow more product generation under equilibrium conditions and hence induce large deformations and stresses. Another consequence of these local deformations is that tensile deformations are observed right above these high compressive stress areas. Tensile in plane stresses are all over the alloy with highest value reached at grain boundary due to maximum depletion. If spallation is caused by nucleation and propagation of microcrack within the oxide or at the interface, the normal stress σ_{22} could play a critical role. Fig. 7 shows the normal stresses σ_{22} in oxide and alloy after 100 h of oxidation. Normal tensile stress of hundred MPa level can be found on both sides of the high compressive area around the oxide/alloy interface. At the alloy side, both tensile stresses and compressive are also found right below the interface. The original for compressive stresses may be from the expansion of oxide at the interface also force the contacted alloy deform compressively. Corresponding normal stresses along the oxide/alloy interface are plotted in Fig. 8 for the purpose of illustration. Even though the tensile stresses are with less magnitude than those of compressive stress, they affect more interface areas. Once depletion induces voids and microcracks, these tensile stresses right around could be the driven forces that assist their propagation. In Fig. 7, high tensile-stress concentration can be found at the grain boundaries

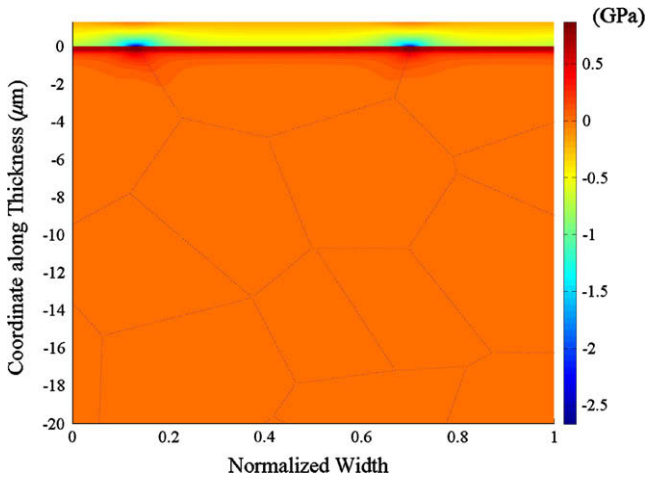

Fig. 6. Contour of in-plane stress σ_{11} in oxide and alloy after 200 h of oxidation.

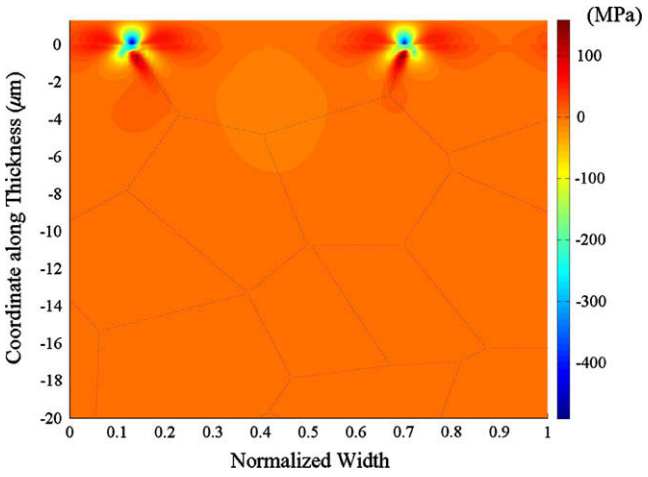

Fig. 7. Contour of normal stress σ_{22} in oxide and alloy after 200 h of oxidation.

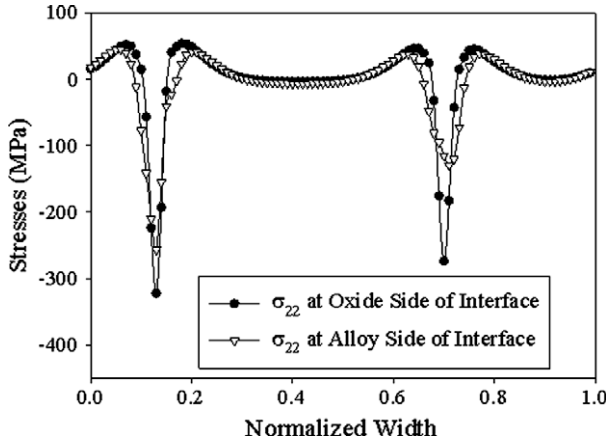

Fig. 8. Normal stresses σ_{22} at metal–oxide interface.

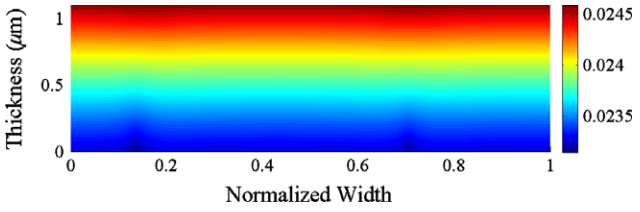

Fig. 9a. Contour of oxygen ion distribution in the oxide.

such that depletion could get expedited there. It has been pointed out [21] that tensile are the cause of void nucleation by triaxiality. Furthermore, high tensile stresses may even induce peel off the whole grain. This may be one of the answers to the generation of the dent areas, including the voiding in grain boundaries, along oxide/alloy interface [7].

Contours of oxygen ion distribution in the oxide are shown in Fig. 9a. The tiny non-uniform distribution in x_1 direction is believed to be the consequences of the distribution of oxidation induced stresses. An interesting phenomenon is shown in Fig. 9b which gives the concentration of oxygen ions along x_1 direction versus different locations along thickness. The concentration at areas adjacent to alloy grain boundaries increases fast and is higher than other areas at short time, and accompanying the oxidation process,

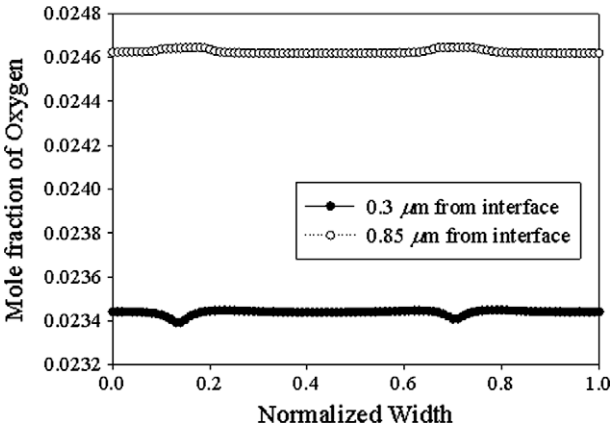

Fig. 9b. The concentration of oxygen ions along x_1 direction versus different locations along thickness.

increases of oxygen ions at these areas switches to a slow rate and eventually lower than those at other areas. Comparing these observation with the stress distribution shown in Figs. 6 and 7, we found that the magnitude of stress gradient affects the ionic diffusion on stresses, which, is consistent with the conclusions of Stephenson [22].

4. Conclusions

In this paper, a 2D finite element implementation of a continuum thermodynamic model accounting for stress-diffusion interaction in the oxidation of Cr–Fe alloys was presented. The advantage of the stress-diffusion coupling model is to provide detailed distribution of stresses, as well as concentration distributions of all diffusing species in the system. The Voronoi tessellation diagram is employed to reflect the real effect mass diffusion among alloy grains and grain boundaries. The model provides clear insight of spallation initiating mechanisms and how the ionic diffusion affects the stress distributions. The presented results confirm the experimental outcomes with predicting that the Cr depletion at alloy boundaries right below the metal–oxide interface. As a consequence of this, normal tensile stresses are generated at both the metal–oxide interface and the alloy grain boundaries. It is believed that those stresses are one of the important driven forces for oxide spallation.

References

[1] J. Stringer, Corros. Sci. 10 (1970) 513–543.
[2] F.N. Rhines, J.S. Wolf, Metall. Mater. Trans. B 1 (1970) 1701–1710.
[3] J.D. Noden, C.J. Knights, M.W. Thomas, Br. Corros. J. 3 (1968) 47–55.
[4] D.R. Clarke, Acta Mater. 51 (2003) 1393–1407.
[5] A.M. Limarga, D.S. Wilkinson, G.C. Weatherly, Scripta Mater. 50 (2004) 1475–1479.
[6] H.G. Zhou, J. Qu, M. Cherkaoui, Mech. Mater. 42 (2010) 63–71.
[7] V.R. Howes, Corros. Sci. 8 (1968) 221–224.
[8] W.M. Pragnell, H.E. Evans, Modell. Simul. Mater. Sci. Eng. 14 (2006) 733–740.
[9] M. Seo, G. Hultquist, F. Baba, N. Sato, Oxid. Met. 25 (1986) 164–174.
[10] S. Kumar, S.K. Kurtz, Acta Metall. Et Mater. 42 (1994) 3917–3927.
[11] Y. Liu, Y. Kageyama, S. Murakami, Int. J. Mech. Sci. 40 (1998) 147–158.
[12] J. Lepinoux, Y. Estrin, Acta Mater. 48 (2000) 4337–4347.
[13] S. Guessasma, Comput. Mater. Sci. 44 (2008) 552–565.
[14] A. Priolo, H.M. Jaeger, A.J. Dammers, S. Radelaar, Phys. Rev. B 46 (1992) 14889–14892.
[15] M. Kamaya, M. Itakura, Eng. Fract. Mech. 76 (2009) 386–401.
[16] F. Fritzen, T. Bohlke, E. Schnack, Comput. Mech. 43 (2009) 701–713.
[17] C. Wagner, J. Electrochem. Soc. 99 (1952) 369–380.
[18] Z.Y. Liu, W. Gao, Y.D. He, Oxid. Metal. 53 (2000) 341–350.
[19] E.A. Garcia, J. Kovacs, J. Nucl. Mater. 210 (1994) 78–83.
[20] H. Kurokawa, K. Kawamura, T. Maruyama, Solid State Ionics 168 (2004) 13–21.
[21] H. El Kadiri, M.F. Horstemeyer, D.J. Bammann, J. Mech. Phys. Solids 56 (2008) 3392–3415.
[22] G.B. Stephenson, Acta Metall. 36 (1988) 2663–2683.